Fernández-Pacheco, Amalio; Vedmedenko, Elena; Ummelen, Fanny; Mansell, Rhodri; Petit, Dorothée; Cowburn, Russell P.

Symmetry-breaking interlayer Dzyaloshinskii–Moriya interactions in synthetic antiferromagnets

Published in:
Nature Materials

DOI:
10.1038/s41563-019-0386-4

Published: 01/07/2019

Document Version
Peer reviewed version

Please cite the original version:
Fernández-Pacheco, A., Vedmedenko, E., Ummelen, F., Mansell, R., Petit, D., & Cowburn, R. P. (2019). Symmetry-breaking interlayer Dzyaloshinskii–Moriya interactions in synthetic antiferromagnets. *Nature Materials*, *18*(7), 679-684. https://doi.org/10.1038/s41563-019-0386-4

Symmetry-Breaking Interlayer Dzyaloshinskii-Moriya Interactions in Synthetic Antiferromagnets

Amalio Fernández-Pacheco [1,2]*, Elena Vedmedenko[3]**, Fanny Ummelen[2,4], Rhodri Mansell[2,5], Dorothée Petit[2], Russell P. Cowburn[2].

[1] SUPA, School of Physics and Astronomy, University of Glasgow, Glasgow G12 8QQ, United Kingdom.

[2] Cavendish Laboratory, University of Cambridge. JJ Thomson Avenue, Cambridge CB3 0HE, United Kingdom.

[3] Institute of Applied Physics, University of Hamburg. Jungiusstr 11 20355 Hamburg, Germany.

[4] Technical University of Eindhoven. 5600 MB Eindhoven, The Netherlands.

[5] Department of Applied Physics, Aalto University School of Science. P.O. Box 15100, 00076 Aalto, Finland.

* amalio.fernandez-pacheco@glasgow.ac.uk

** vedmeden@physnet.uni-hamburg.de

The magnetic interfacial Dzyaloshinskii-Moriya interaction (DMI) in multi-layered thin films can lead to chiral spin states, of paramount importance for future spintronic technologies[1,2]. Interfacial DMI typically manifests as an intralayer interaction, mediated via a paramagnetic heavy metal in systems lacking inversion symmetry[3]. Here we show that, by designing synthetic antiferromagnets with canted magnetisation states[4,5], it is also possible to observe direct evidence of the interfacial interlayer-DMI at room temperature. The interlayer-DMI breaks the symmetry of the magnetic reversal process via the emergence of non-collinear spin states, which results in chiral exchange-biased hysteresis loops. The spin chiral interlayer interactions reported here are expected to manifest in a range of multi-layered thin film systems, opening up as yet unexplored avenues for the development and exploitation of chiral effects in magnetic heterostructures[6–8].

The interfacial Dzyaloshinskii-Moriya interaction (DMI) is an antisymmetric exchange interaction emerging in systems lacking inversion symmetry that promotes chiral coupling between spins[1,3]. In ferromagnets (FM), this gives rise to topological spin textures such as skyrmions and chiral domain walls, with outstanding properties to store, transport and process magnetic information [9–12]. Interfacial DMI in an ultra-thin FM layer describes the coupling of spins $\boldsymbol{S_i}$ and $\boldsymbol{S_j}$, mediated by a paramagnetic (PM) heavy metal atom *l* in a neighbouring layer (left sketch in **Fig. 1a**), as described by the three-site Lévy-Fert model [13]. The DMI energy per atom pair is expressed as $E_{DMI} = \boldsymbol{D_{ij}} \cdot (\boldsymbol{S_i} \times \boldsymbol{S_j})$, where $\boldsymbol{D_{ij}}$ is the Moriya vector, whose direction is dictated by symmetry rules [14]. This interaction favours one sense of rotation of spins in the same FM layer, *i.e.* it is a chiral *intralayer* interaction.

Together with the vast research in FM systems, DMI can potentially play an important role in the emergent field of antiferromanetic (AF) spintronics [8]. In particular, the existence of a non-negligible *interlayer* DMI between neighbouring FM layers separated by a spacer has been recently predicted [15]. Similarly to intralayer-DMI, an interlayer-DMI will lead to the chiral coupling of spins of different FM layers via PM atoms located in an interlayer between both FMs (right sketch in **Fig. 1a**). However, due to the rapid decrease of the DMI interaction with distance and the need for the correct crystallographic symmetry, this effect has not been experimentally observed [16]. Here, we report the experimental observation of a room-temperature chiral exchange bias in SAF bilayers due to the interlayer-DMI, opening an unexplored route for the study and manipulation of chiral spin interlayer interactions in multi-layered spintronic systems.

To obtain experimental evidence of the presence of the interlayer-DMI in synthetic antiferromagnets (SAFs), we have designed magnetic bilayers such as those depicted in **Fig. 1b**, formed by two ultra-thin magnetic layers made of Co and CoFeB, with a heavy metal (Pt) on both sides of the two layers providing perpendicular magnetic anisotropy (PMA) and acting as a source of interfacial DMI. A Ru spacer couples both layers antiferromagnetically via Ruderman-Kittel-Kasuya-Yosida (RKKY) interactions. The Pt layers also tune the magnitude of the effective RKKY coupling. The SAF is magnetically asymmetric: the bottom Co layer is significantly thinner than its spin reorientation transition (SRT), *i.e.* it is magnetically hard, with its magnetisation strongly out-of-plane (z-direction). On the contrary, the top CoFeB layer is slightly thicker than its SRT thickness, with a shape anisotropy moderately larger than its PMA (**Methods**). Thus, the CoFeB layer is a soft magnetic layer which, because of the competition

between its low in-plane anisotropy and the AF coupling with the out-of-plane Co layer, presents canted magnetisation configurations, *i.e.* it has a non-negligible magnetisation component along both in-plane and z directions [4,5]. Furthermore, the application of an in-plane magnetic field during growth breaks the symmetry during deposition (**Supplementary**), providing a moderate in-plane anisotropy along the field direction, referred to as the x-direction in the manuscript.

To estimate the interlayer-DMI strength, the three-site model [13] is applied to our system, represented as three layers arranged in an hexagonal close-packed (hcp) stacking, with two magnetic atom layers separated by a distance t_{IL} from each other by one layer of non-magnetic atoms (**Fig. 1c**). The microscopic intralayer and interlayer DMI vectors $\boldsymbol{D_{ij}}$ are analytically calculated [13] considering only next nearest neighbour FM and nearest neighbour PM atoms (**Methods**). **Fig. 1c** shows the six non-zero resulting $\boldsymbol{D_{ij}^{(Co/Pt/CoFeB)}}$ vectors corresponding to the bonds connecting the central bottom Co spin i and the six outer CoFeB spins j of the top hexagon. From these calculations, the interlayer-DMI strength $|\boldsymbol{D_{ij}^{(Co/Pt/CoFeB)}}|$ is $\approx$ 0.02-0.03V_1, where V_1 *is* the so-called spin-orbit parameter of the material defining the magnitude of the $\boldsymbol{D_{ij}}$ vectors [13,15]. For FM/Pt interfaces, $V_1^{(FM/Pt)} \approx 6.4$ meV/atom [13], of the same order of magnitude as the direct exchange interaction of Co, $J^{(Co)}$ [17]. Hence, $|\boldsymbol{D_{ij}^{(Co/Pt/CoFeB)}}| \approx$ 0.1-0.2 meV/atom, about one order of magnitude smaller than typical values for the intra-layer DMI [18]. The small value of the interlayer-DMI in our samples is mostly due to the relatively large total interlayer thickness of our samples (Pt/Ru/Pt $\approx$ 2 nm) and the decrease of DMI with distance, as described by the three-site model (Methods).

We illustrate the effect of this interaction in the magnetic configuration of a bilayer SAF by depicting the ground state in **Fig. 1d**, for interlayer-DMI as the only (intra- or inter- layer) exchange coupling interaction considered (direct exchange coupling, intra-layer DMI and RKKY are excluded), and for large in-plane CoFeB and out-of-plane Co anisotropies. A strong interlayer-DMI with positive $\boldsymbol{D_{ij}^{(Co/Pt/CoFeB)}}$ results in an anticlockwise rotation between Co and CoFeB spins along the z-direction -from bottom to top- for spins in the same row, and clockwise for spins in adjacent rows. This creates an alternating configuration of spins in both top and bottom layers along the x-direction, as illustrated in Fig. **1e**, where the extended top view of the resulting hexagonal lattice is shown.

The presence of interlayer-DMI has been experimentally investigated under the following vector magnetic fields: First, a strong unipolar -either positive or negative- (~0.4 T) B_z field is applied, saturating both layers. This field is then set to zero, leading to a canted CoFeB layer at remanence. This initialisation is followed by a moderate bipolar oscillating in-plane field (-30 mT < B_x < 30 mT), applied while measuring the reversal of the CoFeB layer. **Figs. 2a-d** shows experiments for one of the samples under investigation following this field sequence, where both M_z (polar MOKE) and M_x (longitudinal MOKE) components of the magnetisation are probed as a function of B_x (**Methods**). Importantly, the hysteresis loops associated to the CoFeB layer reversal are shifted by $B_{bias} \approx \pm 1.1$ mT for the two possible Co orientations.

To complement experimental results, we have performed MC simulations (see **Fig. 1c)** using the atomistic model described in **Methods**. The complex polycrystalline and amorphous crystallographic structure of the sputtered layers, added to unknown spin-orbit parameters, makes it challenging to estimate the DMI values of the samples. Moreover, V_1 will have different values for Co/Pt, Pt/CoFeB and Co/Pt/CoFeB interfaces. To incorporate realistic values in the simulations, we have compared sets of $M_z(B_z)$ experimental results for a wide range of thicknesses with MC simulations (see **Supplementary**). This allows us estimate V_1 for the different interfaces and associate an effective CoFeB thickness t for each sample, given by the $|V_1^{(Pt/CoFeB)}/V_1^{(Co/Pt)}|$ ratio. These estimated spin-orbit parameters are then used in subsequent MC simulations (**Figs. 2e-h**) that replicate the experimental minor loops described before. A good qualitative agreement between experiments and simulations is observed, with simulations reproducing both the shape of the experimental loops and the chiral bias effect. Furthermore, a good quantitative agreement is also found between experiments and simulations when estimating the effective strength of the interlayer-DMI (**Methods**). We therefore conclude that the chiral bias effect described here constitutes a fingerprint of the interlayer-DMI. Other indirect exchange interactions such as the biquadratic interlayer coupling [19] cannot account for the chiral nature of the observed effect. Furthermore, intra-layer DMI effects leading to asymmetric magnetic hysteresis processes have been only observed in laterally-patterned nanomagnets, and require the simultaneous application of orthogonal magnetic fields [20,21], in contast to our experiments.

We have studied the dependence of the chiral $\boldsymbol{B_{bias}}$ magnitude as a function of CoFeB thickness (left and bottom axes in **Fig. 3a**) for the range 1.5 - 2.4 nm. This function rises sharply after the nominal SRT CoFeB thickness, peaking at 1.7 nm, and dropping to negligible values for

thicknesses above 2.2 nm, when the CoFeB becomes strongly in plane. The regime where non-zero B_{bias} is observed corresponds to the thickness range where the CoFeB magnetisation becomes canted [4], as illustrated by the further right axis, where the function $sin2\theta$, as obtained from macrospin MC simulations (**Methods**), presents non-zero values. θ is the effective macrospin canting angle of the CoFeB (see **Fig. 1b**). In addition, the function plotted in nearer-right and top axes is the normalised $|\boldsymbol{B_{bias}}|$ extracted from MC atomistic simulations as a function of the effective CoFeB thickness t, showing an excellent agreement with experiments. **Fig. 3b** displays the characteristic spin configurations of the system, obtained from atomistic simulations, for the thickness ranges: t < 1.6 nm, (AP), 1.6 nm < t < 2.2 nm (CANT) and t > 2.2 nm (PERP). The AP and PERP are standard spin configurations, whereas the spin state for the CANT regime is explained below. No bias is observed for the AP and PERP regimes due to a net zero $E_{DMI}^{(Co/Pt/CoFeB)}$ in both cases (**Methods**). A measureable B_{bias} is only present for the CANT regime, where a small effective CoFeB anisotropy is expected to promote the emergence of effects ruled by small energy contributions, such as the interlayer-DMI.

To understand in detail the CANT regime and its role in the chiral bias, **Fig. 4** includes results from MC simulations for a SAF within this thickness regime. **Fig. 4a** shows snapshots during the reversal process of the CoFeB layer at different B_x values, for Co pointing along the +z direction. Overall, the magnetisation process follows the same mechanism previously reported for this type of samples [4], result of the competing energies present in the system: The soft layer (CoFeB) reverses back and forth under B_x, while the hard (Co) layer remains unchanged because of its high PMA. The AF RKKY promotes an antiparallel orientation of CoFeB and Co, leading to a peak in M_z during CoFeB reversal (**Fig. 2g**). The AF RKKY also results in an incomplete in-plane saturation of CoFeB at the maximum B_x applied (**Fig. 2h**). In addition, the intralayer-DMI promotes a chiral clockwise spin rotation -from left to right- across the CoFeB layer. To satisfy this requirement, the magnetisation reverses via the propagation of domain walls with clockwise chirality. To achieve the same wall chirality for both branches of the hysteresis loop and keep an antiparallel alignment with Co, a domain wall is nucleated at opposite edges of the simulated area for either branch. However, none of these contributions is able to create a biased switching in extended structures and under B_x only [21], requiring an additional symmetry-breaking mechanism. The reversal process will be in reality strongly influenced by defects and inhomogeneities of the layers [22], and driven by domains of very small sizes for thicknesses

around the SRT [23], making their direct observation using magneto-optical methods as those used here very challenging [5]. Despite these, the macroscopic bias observed experimentally indicates that a clear reversal asymmetry for both branches is present.

Complementing these results, **Figs. 2i-j** show the evolution of $E_{DMI}^{(Co/Pt/CoFeB)}$ during CoFeB reversal, for the two possible z-directions of Co. Whereas standard magnetic energy terms are symmetric under inversion of B_x, this is not the case for $E_{DMI}^{(Co/Pt/CoFeB)}$, which presents two plateaus at moderate B_x values and a biased switching. An asterisk in those graphs marks the state of the system that is energetically more favourable from an interlayer-DMI point of view, which is depicted in the insets of **Figs. 2f-h**. These sketches show the spin configuration for top CoFeB and bottom Co layers, where green (red) interconnecting lines indicate the pair bonds where the interlayer-DMI is energetically favourable (unfavourable) for that spin configuration (compare with **Fig. 1d**). The figure also indicates how unfavourable bonds cause canting of the CoFeB spins (red arrows) which become more antiparallel to Co because of the strong AF RKKY interaction.

MC simulations evidence the emergence of this type of noncollinear magnetisation states, as a result of the competition between interlayer-DMI and RKKY coupling (**Fig. 4b**). Magnetisation amplitude changes of up to 15% for S_x, with a period corresponding to a few atomic lattice constants, are observed in simulations, with this behavior dependent on the $|V_1^{(Pt/CoFeB)}|/|V_1^{(Co/Pt)}|$ ratio (not shown here). The relevance of noncollinear magnetic phases for symmetry breaking has already been pointed out [24]. Here, simulations indicate how this CoFeB magnetisation modulation is different for either branch, due to the different configuration of -energetically satisfied and unsatisfied- interlayer-DMI bonds for either branch (**Fig. 4(c,d)**). The subtle symmetry breaking mechanism responsible for the chiral exchange bias is thus the result of these two effects acting together: the emergence of noncollinear spin states during reversal, combined with this asymmetric bond profile. This magnetisation modulation asymmetry also manifests as other small asymmetric features in these loops. For instance, the M_z peak reaches larger values for one of the two branches (**Figs. 2e, g**), revealing spin modulations of larger amplitude, due to the interlayer-DMI competing less efficiently with the RKKY interaction.

In conclusion, we report a room temperature chiral exchange bias in ultra-thin asymmetric synthetic antiferromagnetic bilayers caused by the presence of DMI across the interlayer. The

emergence of noncollinear spin modulation, subject to different interlayer-DMI profiles during magnetic reversal, is behind this symmetry breaking. Whereas the interlayer-DMI would appear to be too weak to significantly change the intralayer magnetic ordering, due to the competition with a strong direct exchange and intralayer-DMI contributions, it can however be effective in competition with RKKY coupling, co-defining the interlayer ordering.

The canted SAFs studied here have been specifically designed to probe the presence of the interlayer-DMI, which manifests as a macroscopic chiral exchange bias. However, we expect symmetry-breaking effects induced by this interaction to play an important role in other ultra-thin SAFs away from the SRT and with more standard magnetic configurations. Specifically, provided that the symmetry arguments exposed here are fulfilled, the interlayer-DMI will become important in these systems when the magnetic reversal becomes dominated by areas with a low effective anisotropy, such as defects and layer inhomogeneities[25]. Moreover, larger net interlayer-DMI energies than the one reported here are expected in other multilayered systems formed by ultra-thin interlayers (see Methods), including *e.g.* the use of spacer materials that simultaneously present both RKKY and DMI interactions[26]. This interaction will also be of particular importance in magnetic systems with large antisymmetric/symmetric exchange interaction ratios[27]. The realisation of systems integrating interlayer magnetic chiral interactions paves the way for the creation and manipulation of unprecendented magnetic effects in synthetic antiferromagnets, *e.g.* the introduction of indirect -via the magnetic state of a neighbouring layer- control of asymmetric effects in the motion of domain walls[28] and spin waves[29] of a magnetic system. It is also of great relevance towards the development of future three-dimensional spintronic systems [6,7].

Data availability:

All data associated to this publication is available via Enlighten, the University of Glasgow public repository.

References:

1. Wiesendanger, R. Nanoscale magnetic skyrmions in metallic films and multilayers: a new twist for spintronics. *Nat. Rev. Mater.* **1,** 16044 (2016).
2. Sander, D. *et al.* The 2017 Magnetism Roadmap. *J. Phys. D. Appl. Phys.* **50,** 363001 (2017).
3. Hellman, F. *et al.* Interface-induced phenomena in magnetism. *Rev. Mod. Phys.* **89,** 025006 (2017).

4. Ummelen, F. C. *et al.* Controlling the canted state in antiferromagnetically coupled magnetic bilayers close to the spin reorientation transition. *Appl. Phys. Lett.* **110,** (2017).

5. Fernández-Pacheco, A. *et al.* Dynamic selective switching in antiferromagnetically-coupled bilayers close to the spin reorientation transition. *Appl. Phys. Lett.* **105,** (2014).

6. Lavrijsen, R. *et al.* Magnetic ratchet for three-dimensional spintronic memory and logic. *Nature* **493,** 647–50 (2013).

7. Fernández-Pacheco, A. *et al.* Three dimensional nanomagnetism. *Nat. Commun.* **8,** 15756 (2017).

8. Baltz, V. *et al.* Antiferromagnetic spintronics. *Rev. Mod. Phys.* **90,** 015005 (2018).

9. Woo, S. *et al.* Observation of room-temperature magnetic skyrmions and their current-driven dynamics in ultrathin metallic ferromagnets. *Nat. Mater.* **15,** 501–506 (2016).

10. Boulle, O. *et al.* Room-temperature chiral magnetic skyrmions in ultrathin magnetic nanostructures. *Nat. Nanotechnol.* **11,** 449–454 (2016).

11. Jué, E. *et al.* Chiral damping of magnetic domain walls. *Nat. Mater.* **15,** 272–277 (2015).

12. Ryu, K.-S., Thomas, L., Yang, S.-H. & Parkin, S. Chiral spin torque at magnetic domain walls. *Nat. Nanotechnol.* **8,** 527–533 (2013).

13. Levy, P. M. & Fert, A. Anisotropy induced by nonmagnetic impurities in Cu Mn spin-glass alloys. *Phys. Rev. B* **23,** 4667–4690 (1981).

14. Crépieux, A. & Lacroix, C. Dzyaloshinsky–Moriya interactions induced by symmetry breaking at a surface. *J. Magn. Magn. Mater.* **182,** 341–349 (1998).

15. Vedmedenko, E. Y., Arregi, J. A., Riego, P. & Berger, A. Interlayer Dzyaloshinskii-Moriya interactions. *arXiv:1803.10570v2* (2018).

16. While writing this manucript, we became aware of this other publication reporting experimental 325 evidence of a chiral bias in SAFs that the authors associate to the interlayer DMI: D.-S. Han *et al.*, 326 Chiral magnetic interlayer coupling in synthetic antiferromagnets: Han, D.-S. *et al.* Chiral magnetic interlayer coupling in synthetic antiferromagnets. *arXiv:1809.01080v1* (2018).

17. Dupé, B., Hoffmann, M., Paillard, C. & Heinze, S. Tailoring magnetic skyrmions in ultra-thin transition metal films. *Nat. Commun.* **5,** 4030 (2014).

18. Yang, H., Thiaville, A., Rohart, S., Fert, A. & Chshiev, M. Anatomy of Dzyaloshinskii-Moriya Interaction at Co / Pt Interfaces. *Phys. Rev. Lett.* **115,** 267210 (2015).

19. Ives, A. J. R., Bland, J. A. C., Hicken, R. J. & Daboo, C. Oscillatory biquadratic coupling in Fe/Cr/Fe(001). *Phys. Rev. B* **55,** 12428–12438 (1997).

20. Han, D. S. *et al.* Asymmetric hysteresis for probing Dzyaloshinskii-Moriya interaction. *Nano Lett.* **16,** 4438–4446 (2016).

21. Pizzini, S. *et al.* Chirality-Induced Asymmetric Magnetic Nucleation in Pt / Co / AlO x Ultrathin Microstructures. *Phys. Rev. Lett.* **113,** 047203 (2014).

22. Lee, J.-H. *et al.* Domain imaging during soliton propagation in a 3D magnetic ratchet. *SPIN* **03,** 1340013 (2013).

23. Kisielewski, M. *et al.* Drastic changes of the domain size in an ultrathin magnetic film. *J. Appl. Phys.* **93,** 6966–6968 (2003).

24. Kimura, T., Lashley, J. C. & Ramirez, A. P. Inversion-symmetry breaking in the noncollinear magnetic phase of the triangular-lattice antiferromagnet Cu Fe O 2. *Phys. Rev. B* **73,** 220401

(2006).

25. Ferré, J. *et al.* Magnetization-reversal processes in an ultrathin Co/Au film. *Phys. Rev. B* **55,** 15092–15102 (1997).

26. Liu, Y., Zhou, B. & Zhu, J.-G. Field-free Magnetization Switching by Utilizing the Spin Hall Effect and Interlayer Exchange Coupling of Iridium. *Sci. Rep.* **9,** 325 (2019).

27. Romming, N. *et al.* Competition of Dzyaloshinskii-Moriya and Higher-Order Exchange Interactions in Rh / Fe Atomic Bilayers on Ir(111). *Phys. Rev. Lett.* **120,** 207201 (2018).

28. Shahbazi, K. *et al.* Domain-wall motion and interfacial Dzyaloshinskii-Moriya interactions in Pt / Co / Ir (t Ir) / Ta multilayers. *Phys. Rev. B* **99,** 094409 (2019).

29. Di, K. *et al.* Asymmetric spin-wave dispersion due to Dzyaloshinskii-Moriya interaction in an ultrathin Pt/CoFeB film. *Appl. Phys. Lett.* **106,** 052403 (2015).

30. Wiese, N. *et al.* Antiferromagnetically coupled CoFeB/Ru/CoFeB trilayers. *Appl. Phys. Lett.* **85,** 2020 (2004).

31. Lavrijsen, R. *et al.* Tuning the interlayer exchange coupling between single perpendicularly magnetized CoFeB layers. *Appl. Phys. Lett.* **100,** 052411 (2012).

32. Raanaei, H. *et al.* Imprinting layer specific magnetic anisotropies in amorphous multilayers. *J. Appl. Phys.* **106,** 023918 (2009).

33. Kang, S. P. *et al.* The spin structures of interlayer coupled magnetic films with opposite chirality. *Sci. Rep.* **8,** 2361 (2018).

34. Eyrich, C. *et al.* Exchange stiffness in thin film Co alloys. *J. Appl. Phys.* **111,** 07C919 (2012).

35. Perini, M. *et al.* Domain walls and Dzyaloshinskii-Moriya interaction in epitaxial Co/Ir(111) and Pt/Co/Ir(111). *Phys. Rev. B* **97,** 184425 (2018).

Methods

Synthetic antiferromagnets: The samples studied here were grown by DC magnetron sputtering, under a base pressure of 7×10^{-8} mbar and a growth pressure of 8×10^{-3} mbar. The structure is Ta(4.0 nm)/Pt(10.0 nm)/Co(1 nm)/Pt(0.5 nm)/Ru(1.0 nm)/Pt(0.5 nm)/$Co_{60}Fe_{20}B_{20}$(1.6-2.4 nm)/Pt(2.0 nm)/Ta(2.0 nm). The Ru spacer provides antiferromagnetic coupling between the two ferromagnetic films via RKKY interaction [30]. Although only one Pt layer at the interlayer is in principle needed to observe interlayer-DMI, a symmetric interlayer with two Pt interfaces was used to improve the PMA of the FM layers, as well as to provide fine tuning over the RKKY coupling between the two[31]. The surface PMA of the Co and CoFeB layers, determined by growing single layers with analogous structure, are 1.2 mJ/m^2 and 0.7 mJ/m^2. This corresponds to SRT thicknesses of ≈ 1.95 nm for Co and 1.55 nm for CoFeB, when the shape anisotropy balances the surface PMA, *i.e.* when the effective anisotropy $K_{eff} = 2K_s/t - 0.5\ \mu_0 M_s^2 = 0$. RKKY coupling is created by a 1 nm Ru layer, which corresponds to the first AF peak, and tuned by the Pt on both sides. For 0.5 nm of Pt, this corresponds to an AF surface energy $J_{RKKY}^{(Co/Ru/CoFeB)}$ of -

0.08 mJ/m^2. A magnetic field of ≈ 100 mT is applied during the sputtering process, resulting in a moderate in-plane anisotropy for the CoFeB layer along the field direction [32], measured to be up to 1.8 × 10^3 J/m^3. A chiral bias effect has also been observed in another similar set of samples (**Supplementary**).

Atomistic Three-Site Model: The interlayer-DMI effect is modelled using a FM_1/PM/FM_2 atomistic trilayer with hcp stacking. The z-position of each atomic plane corresponds effectively to the middle point of each layer [33]. Each magnetic layer is represented by a single monolayer of Heisenberg spins $\boldsymbol{S_i}$ and $\boldsymbol{S_j}$ at atomic positions $\boldsymbol{R_i}$ and $\boldsymbol{R_j}$. The spin-orbit parameters for the bottom and top layers are defined as $V_l^{(Co/Pt)}$ and $V_l^{(Pt/CoFeB)}$, respectively, and between layers as $V_l^{(Co/Pt/CoFeB)}$. Microscopic DMI vectors describing the interaction between spins $\boldsymbol{S_i}$ and $\boldsymbol{S_j}$ as mediated by impurity l within and in-between layers are obtained using the three-site model [13]:

$$\boldsymbol{D_{ijl}}(\boldsymbol{R}_{li}, \boldsymbol{R}_{lj}, \boldsymbol{R}_{ij}) = -V_1 \frac{sin\left(k_F(R_{li}+R_{lj}+R_{ij})+(\pi/10)Z_d\right)(\boldsymbol{R_{li}}\cdot\boldsymbol{R_{lj}})(\boldsymbol{R_{li}}\times\boldsymbol{R_{lj}})}{|R_{li}|^3|R_{lj}|^3 R_{ij}}, \quad (1)$$

where $\boldsymbol{R_{li}}$, $\boldsymbol{R_{lj}}$ are the distance vectors from the impurity l to the corresponding FM atom sites i and j, and $\boldsymbol{R_{ij}}$ the distance vector between these FM sites. The parameter $V_1 = \frac{135\pi}{32}\frac{\lambda_d \Gamma^2}{E_F^2 k_F^3} sin\left(\frac{\pi}{10}Z_d\right)$ refers to the material specific quantity defining the DMI strength. Hereby, k_F and E_F are the Fermi wave vector and energy respectively, λ_d is the spin-orbit coupling parameter, Γ the interaction parameter between the localised spins and the spins of conduction electrons, and Z_d the number of d-electrons.

An effective DMI vector describing the interaction between a given ij atomic pair can be calculated by performing a sum over all nearest neighbour PM impurities l [13,15]:

$$\boldsymbol{D_{ij}^{eff}} = \sum_l \boldsymbol{D_{ijl}}(\boldsymbol{R_{li}}, \boldsymbol{R_{lj}}, \boldsymbol{R_{ij}}) \quad (2)$$

The total DMI energy between two magnetic layers is then given by

$$E_{DMI} = \sum_{ij} \boldsymbol{D_{ij}^{eff}} \cdot (\boldsymbol{S_i} \times \boldsymbol{S_j}) \quad (3)$$

where this time, next-nearest neighbour ij pairs are considered in the calculations.

If we evaluate equation (3) for the three thickness regimes discussed in **Fig. 3b**, we find that the AP configuration obviously leads to zero interlayer-DMI, due to both layers forming 180^o, resulting in $\boldsymbol{S_i} \times \boldsymbol{S_j} = 0$ for all pairs. The net interlayer-DMI is also zero in the PERP configuration, despite Co and CoFeB spins forming 90^o. In that case, equation (3) becomes

$$E_{DMI} = \left(\boldsymbol{S_i} \times \boldsymbol{S_j}\right) \cdot \sum_{ij} \boldsymbol{D_{ij}^{eff}} = 0 \quad (4)$$

since $(\boldsymbol{S_i} \times \boldsymbol{S_j})$ is the same for each pair, and the total sum of $\boldsymbol{D_{ij}^{eff}}$=0 for an hexagonal lattice. However, noncolinear spin configuration in the soft CoFeB layer (CANT configuration) will result in a non-zero DMI energy as describes by eq (3).

The arguments presented here for hcp stacking can be also extended to other crystallographic structures. A net non-zero $\boldsymbol{D_{ij}^{(Co/Pt/CoFeB)}}$ vector is obtained, for instance, for distorted or disordered cubic phases [15]. **Supplementary** includes additional information about the atomistic model.

Magnetometry measurements: The samples were investigated using focused magneto-optical Kerr effect, with a 3.5 mW laser Gaussian spot of FWHM ≈ 5 μm and wavelength = 635 nm. To probe both M_z and M_x components of the samples, two different setups were used, with either normal or 45° incidence geometries. Optical analyser and quarter-wave plate angles were tuned to detect either Polar or Longitudinal Kerr signals, respectively.

Analogous (bulk) vibrating sample magnetometer (VSM) measurements with two sets of perpendicular pick-up coils and Kerr control experiments complement these measurements (**Supplementary**).

Monte Carlo atomistic simulations: As a complement to analytical calculations, we perform atomistic MC simulations using the model Hamiltonian

$$H = -\sum_{ij} J^{(\mathrm{Co})}(\boldsymbol{S_i} \cdot \boldsymbol{S_j}) - \sum_{ij} J^{(\mathrm{CoFeB})}(\boldsymbol{S_i} \cdot \boldsymbol{S_j}) - \sum_{\mathrm{ij}} J_{ij}^{\mathrm{RKKY}}(\boldsymbol{S_i} \cdot \boldsymbol{S_j}) - K_i^{(Co)} \sum_i (S_i^z)^2 - K_i^{(CoFeB)} \sum_i (S_i^x)^2 - \sum_{ij} \boldsymbol{D_{ij}^{eff}}(\boldsymbol{S_i} \times \boldsymbol{S_j}) \quad (5)$$

based on experiments and typical parameters of Co-based alloys[34]: A strong PMA is included for the bottom Co layer, $K_i^{(Co)} \approx K_z^{(Co)} \approx 0.7\ J^{(Co)}$, and the top CoFeB layer is close to the SRT, $K_z^{(CoFeB)} \approx 0$. Additionaly, we introduce an additional in-plane anisotropy in this layer to mimic experiments: $K_x^{(CoFeB)} \approx 0.4\ J^{(CoFeB)}$. The FM intralayer exchange interaction for both layers is set as $J^{(CoFeB)}/J^{(Co)} = 0.5$ and the AF RKKY coupling between both layers as $J_{ij}^{RKKY} = -0.1\ J^{(Co)}$.

Samples with lateral dimensions of up to 50a × 50a on an hcp lattice with periodic and open boundaries have been considered. Calculations have been performed for a wide of temperatures kT =0.05-0.1 $J^{(Co)}$. The Monte Carlo simulations are used to calculate magnetisation curves, comparing them with experimental data. This allows us to access to the atomic-scale configuration during magnetisation reversal. For calculations of the $M_x(B_x)$ curves, out-of-plane Co and in-plane CoFeB magnetic orientations were used as the initial configuration, whereas

fully saturated out-of-plane states were used as the initial state for $M_z(B_z)$ loops (**Supplementary**). In the simulations, 10^5 MC initial steps were used first to reach magnetic equilibrium. After those, the magnetisation curves were recorded by sweeping over the lattice at every MC step, updating the orientations of the spins following single-spin Metropolis dynamics. At every field, the system was again thermalised for 10^5 steps, then the averaging was performed.

Monte Carlo macrospin simulations: Macrospin MC simulations were carried out to determine the effective canting angle of the CoFeB layer as a function of its thickness, for the SAF under investigation. PMA, in-plane shape anisotropy and RKKKY AF coupling were considered (*i.e.* neither type of DMI is included). The parameters used were extracted from experiments. PMA: $K_s^{(Co)} = 1.2$ mJ/m^2, $K_s^{(CoFeB)} = 0.7$ mJ/m^2. In-plane volume anisotropy: $K_v^{(CoFeB)} = 1.8 \times 10^2$ J/m^3 . Spontaneous magnetisation: $M_s^{(Co)} = 1.4 \times 10^6$ A/m, $M_s^{(CoFeB)} = 1.2 \times 10^6$ A/m. $J_{RKKY}^{(Co/Ru/CoFeB)} =$ -0.08 mJ/m^2.

Estimation of the interlayer-DMI from the magnitude of the bias field: Since the interlayer-DMI is considered as the only symmetry-breaking source in the system, $|\boldsymbol{B}_{bias}|$ can be identified with the effective strength of the interlayer-DMI. Hence, *e.g.* a bias of 1 mT for the 2.1 nm thick CoFeB corresponds to an effective energy of 10^{-4} meV/atom, given by $E_{DM}^{(Co/Pt/CoFeB)} = m|\boldsymbol{B}_{bias}|$ $\approx 2\ \mu_B$ /atom $\times$ 1 mT $\approx 10^{-4}$ meV/atom, with m the magnetic atomic moment, expressed in units of the Bohr magneton μ_B. This compares with the bias energy extracted from simulations for hcp stacking with interlayer distance $t_{IL}=2a\sqrt{2/3} = 0.4$ nm for a lattice constant $a = 0.25$ nm (**Figs. 2(i,j)**) in the main manuscript): $E_{DM}^{(Co/Pt/CoFeB)} = mB_{bias} \sim 0.001\ J^{(Co)} \approx 2 \times 10^{-2}$ meV/atom, if $J^{(Co)} \approx 20$ meV/atom is considered [17,35]. If we consider instead $t_{IL} = 8\ a\sqrt{2/3}$, ≈ 2 nm as in experiments, an interlayer- DMI energy of 5×10^{-4} meV/bond is obtained. This is in rather good agreement with the experimental $|\boldsymbol{B}_{bias}|$, despite the difference between the complex experimental system investigated, comprising polycrystalline/amorphous sputtered samples and rough interfaces, in contrast with the model, where a perfect crystalline hcp structure has been considered.

Raw data and Monte Carlo codes

All metadata for this publication is available via the following link: http://dx.doi.org/10.5525/gla.researchdata.787. The atomistic and macrospin Monte Carlo codes used for this study are available from the corresponding authors on reasonable request.

Acknowledgments:

We acknowledge fruitful discussions with Nicolas Jaouen, Stefan Stanescu and Aurelio Hierro-Rodríguez, as well as experimental support from Dédalo Sanz Hernández, Alexander Welbourne, Peter Seem and Ian Farrer. AFP acknowledges funding from an EPSRC Early Career Fellowship EP/M008517/1, and from the Winton Program for the Physics of Sustainability. EV from Horizon 2020 research and innovation program under Grant Agreement No. 665095 (MAGicSky). DP and RPC from the Templeton World Charity Foundation. FU thanks the Erasmus Mobility program.

Author contributions: AFP designed and carried out the experiments, grew the samples, analysed the data, did the MC macrospin simulations and wrote the manuscript. EV performed the analytical calculations, did the atomistic MC simulations and analysed the data derived from them, and wrote the manuscript. FU grew samples and analysed data. RM contributed to the experimental characterization of the samples. All authors discussed and contributed to the interpretation of the results, as well as to the writing of the manuscript.

Competing interests:

Authors declare no competing interests.

Materials and correspondences:

For correspondence and materials request, contact:

amalio.fernandez-pacheco@glasgow.ac.uk

vedmeden@physnet.uni-hamburg.de

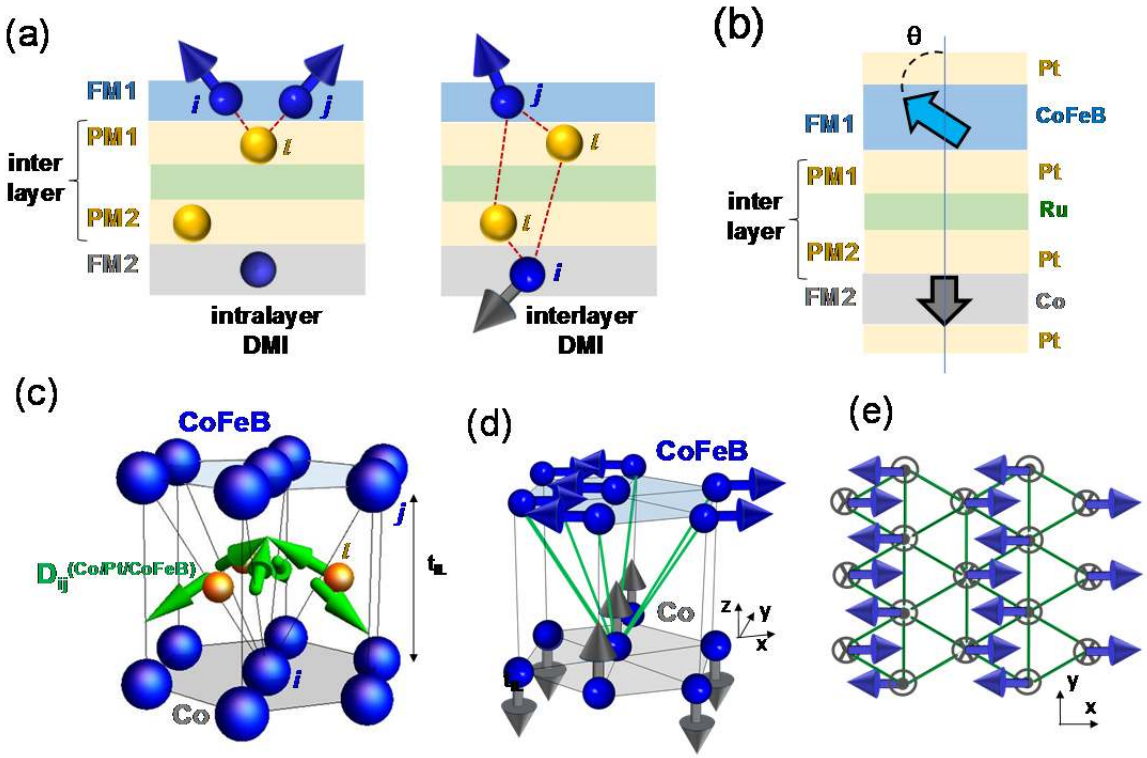

Fig. 1. Interlayer-Dzyaloshinskii-Moriya Interaction (DMI) investigations in canted synthetic antiferromagnets (SAFs). (a) Left. Intralayer-DMI coupling between spins *i* and *j* of the same ferromagnetic (FM) layer via a paramagnetic (PM) atom; the figure depicts this type of coupling for the top FM layer only. **Right.** Interlayer-DMI coupling (right) between spins of two neighbouring FM layers separated by a spacer, mediated by PM atoms. **(b)** Schematic of the magnetic state at remanence of the SAFs studied in a macrospin approximation: two ultra-thin CoFeB (top) and Co (bottom) layers with Pt at the interfaces, separated by Ru to create antiferromagnetic coupling between both FM layers via Ruderman-Kittel-Kasuya-Yosida (RKKY) interaction. The two FM layers have different proximities to their corresponding spin-reorientation-transition, with Co remaining out-of-plane and CoFeB becoming canted with respect to the substrate plane. θ is the (polar) effective macrospin canting angle of this layer. **(c)** $\boldsymbol{D}_{ij}^{(Co/Pt/CoFeB)}$ interlayer-DMI vectors (green) calculated via the 3-sites model for a Co(i)/Pt(*l*)/CoFeB(*j*) trilayer with hexagonal close-packed (hcp) structure. The distance between magnetic atoms is the interlayer thickness (t_{IL})**.** The *j* letter denotes one of the seven next-nearest neighbours of the *i* central bottom spin, with *l* the corresponding PM atom for this bond included in the calculations. The $\boldsymbol{D}_{ij}^{(Co/Pt/CoFeB)}$ vector corresponding to the interaction between both central atoms at top and bottom hexagons equals zero when computed across the three nearest neighbour impurities. **(d)** Ground state spin configuration based solely on the interlayer-DMI, for a hexagonal-closed-packed trilayer with in-plane top and out-of-plane bottom magnetisations (no FM direct or AF RKKY exchange is considered). All green bonds connecting the middle Co to the outer CoFeB spins are interlayer-DMI energetically favourable. **(e)** Extended top view of the hexagonal lattice for the same ground state as in (d). x is the direction of the CoFeB in-plane anisotropy.

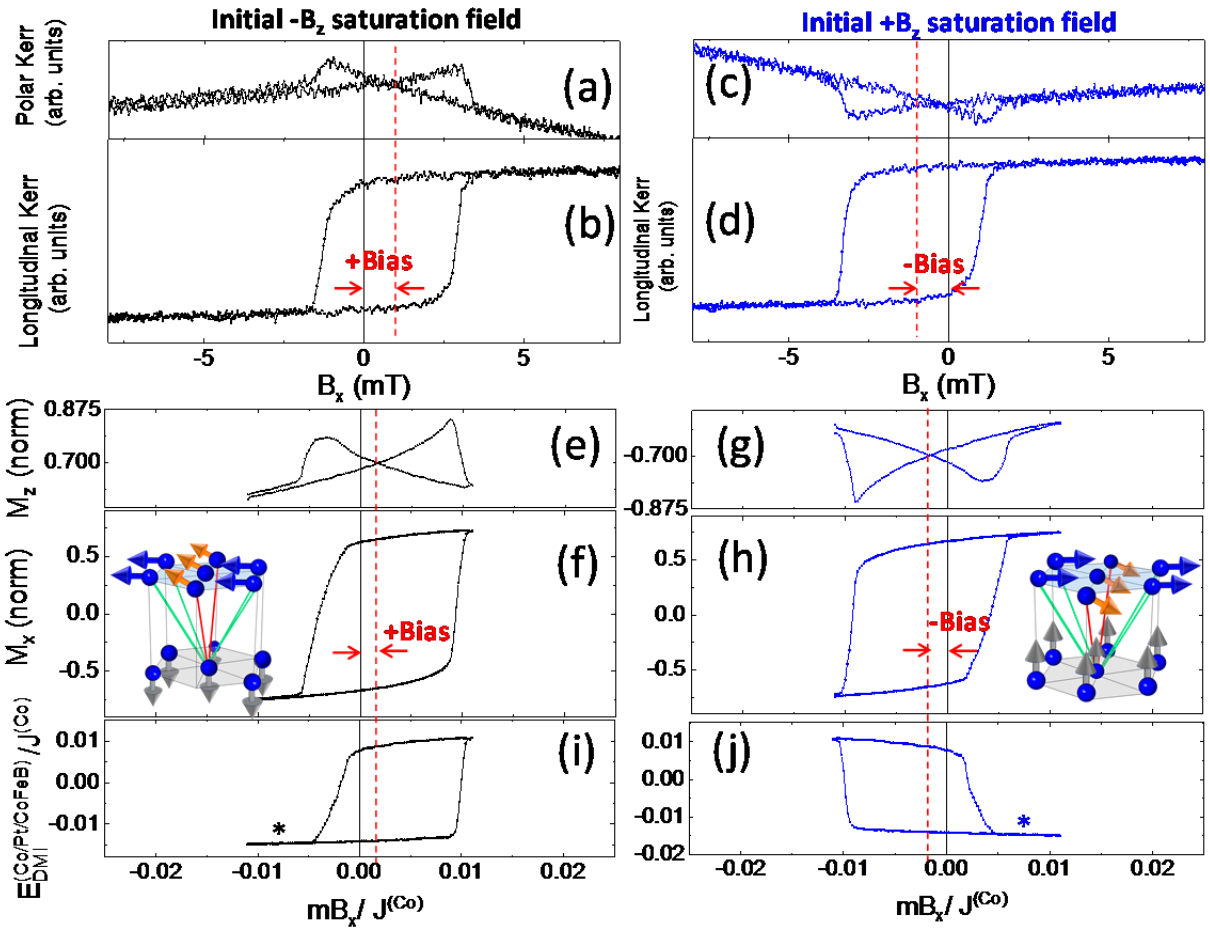

Fig. 2. Chiral exchange bias due to the interlayer-DMI. (a-d) Chiral exchange bias observed during the reversal of the canted CoFeB layer, for a sample with CoFeB thickness = 2.1 nm. The magnetisation components M_z (a,c) and M_x (b,d) of the CoFeB film are measured by Kerr effect under B_x magnetic fields, after negative (a,b) and positive (c,d) initial saturating orthogonal B_z fields that define the magnetic state of the Co layer for the rest of the field sequence. This magnetic field sequence is thus a minor loop used to probe the reversal of the canted free layer, while the out-of-plane layer remains fixed along the z-direction. The bias effect, obtained from the switching field (M_x) and peaks (M_z), is marked by a red dashed line. The insets show the most favourable state of the two under moderately high B_x fields, based on the interlayer-DMI; red/green lines denote interlayer-DMI energetically unfavourable/favourable bonds connecting j top outer spins to the central i bottom spin. Canted spins promoted by the RKKY interaction and an unfavourable interlayer-DMI are colored in red, in contrast to blue spins, where the two interactions promote instead an in-plane spin configuration. **(e-h)** Monte Carlo atomistic simulations reproducing the experiments, with $V_1^{(Pt/CoFeB)}/V_1^{(Co/Pt)}$ = 1.7, corresponding to a CoFeB thickness t = 2.1 nm. **(i, j)** Evolution of the interlayer-DMI energy $E_{DMI}^{(Co/Pt/CoFeB)}$ during the hysteresis loops; an asterisk marks the states sketched in the inset of (f) and (h). Both mB_x and interlayer-DMI energies are normalised with respect to $J^{(Co)}$, the direct intralayer exchange energy, with m the magnetic moment of the system.

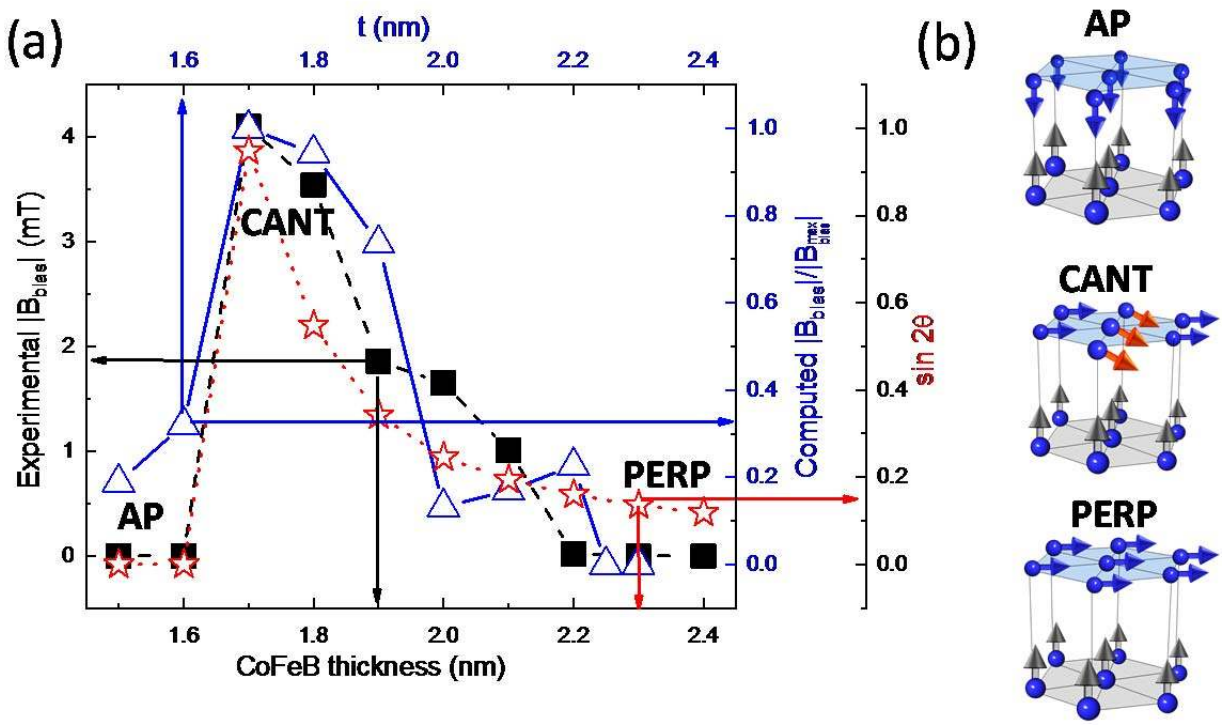

Fig. 3. Bias field dependence with CoFeB thickness. (a) Left, bottom axes (black squares and dashed line) are experiments, showing a peak around the spin reorientation transition (SRT). **Nearer-right, top axes** (blue triangles and dash-dot line) show computed normalised bias from atomistic MC simulations, with *t* the effective CoFeB thickness, corresponding to an interval of $|V_1^{(Pt/CoFeB)}/V_1^{(Co/Pt)}|$ between -1.7 and +1.9 (**Supplementary**). The same behaviour is evidenced for experiments and simulations. **Further-right, bottom axes** (red stars and dotted line) plots the effective degree of canting of the CoFeB layer (when it is neither in-plane nor out-of-plane) as a function of its thickness, parametrised as $sin2\theta$, as extracted from macrospin MC simulations; only anisotropies and RKKY coupling interactions are considered. The magnitude of the bias correlates well with the magnetisation effective degree of canting of the CoFeB layer, revealing that a low competing effective anisotropy is necessary to observe a bias effect. **(b)** Schematics of the three types of spin configurations: antiparallel (AP), canted (CANT), and perpendicular (PERP) across the SRT. A non-zero net interlayer-DMI is only present for the CANT regime. Red spins in the CANT state are those more favourable to become out-of-plane, due to an energentically unfavourable interlayer-DMI and the effect of the RKKY interaction.

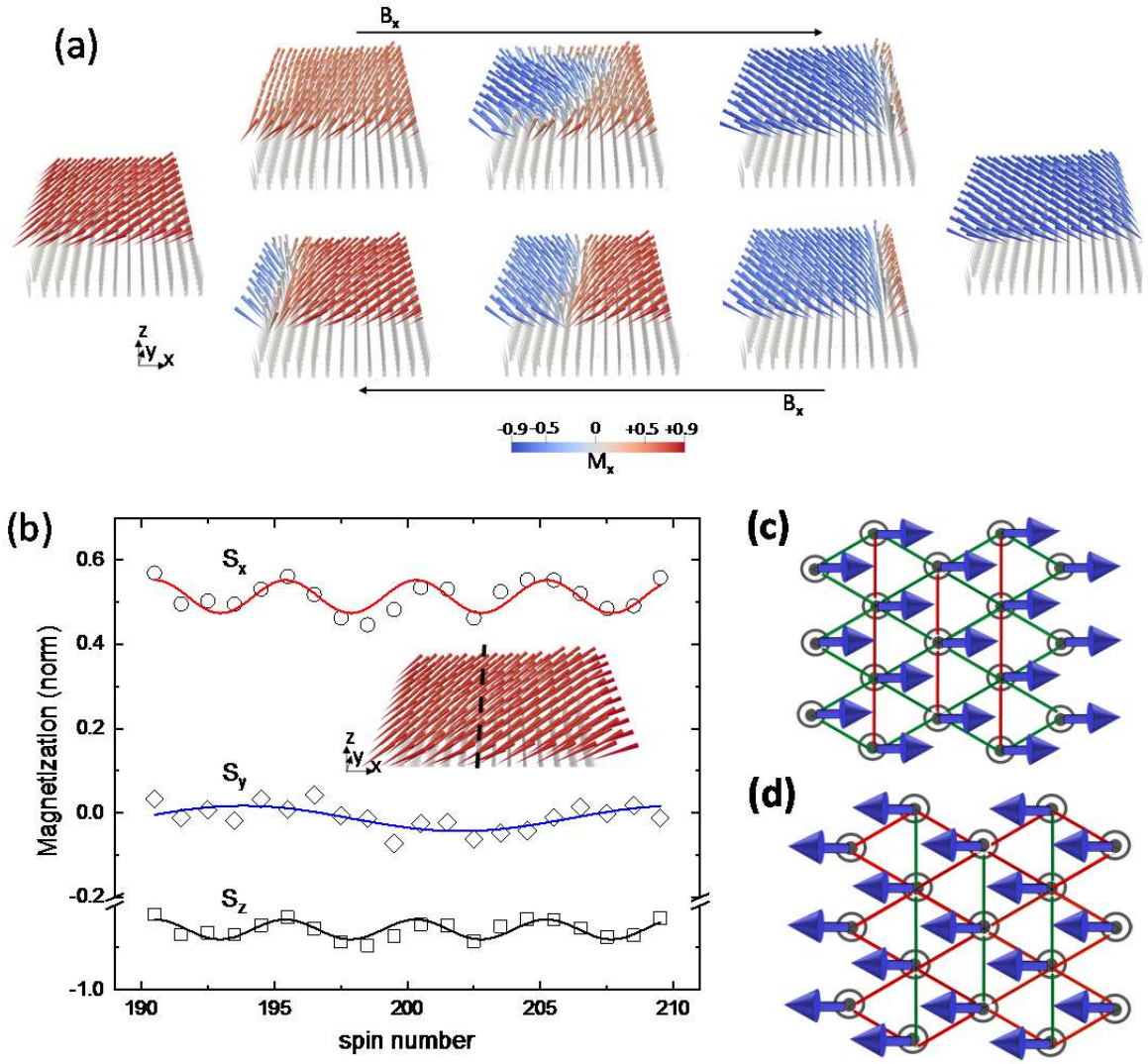
(a)
B_x
z
y
x
B_x
-0.9 -0.5 0 +0.5 +0.9
M_x
(b)
Magnetization (norm)
0.6
0.4
0.2
0.0
-0.2
-1.0
S_x
S_y
S_z
190
195
200
205
210
spin number
(c)
(d)

469

Fig. 4. Emergence of spin modulations. **(a)** Snapshots of Monte Carlo simulations at remanence for a SAF with an effective CoFeB thickness = 2.1 nm and Co pointing upwards. Figs. 2(g,h) are the corresponding hysteresis loops. Forward (top) and backward (bottom) branches of the B_x hysteresis loop are included. Top spins in red and blue indicate the value of M_x for the top CoFeB layer during reversal. The grey bottom spins represent the Co layer along +z. The reversal process is asymmetric for both loop branches and occurs at different magnetic fields, resulting in a biased hysteresis loop. **(b)** Three components of the magnetisation as a function of the atomic spin number across the dashed line in the inset, for $B_x = 0$ and starting from negative fields. Periodic changes in the amplitude of the three components in the simulations reveal the presence of spin modulations in the CoFeB layer. Different periods for the three components are observed due to their anharmonic character. **(c,d)** Top extended view of the hexagonal lattice, with bottom Co spins colored in grey and CoFeB top spins in blue. $E_{DMI}^{(Co/Pt/CoFeB)} = 0$ for both spin configurations. However, a different number and symmetry of favourable (green) and unfavourable (red) interlayer-DMI bonds is obtained for (b) and (c), breaking the symmetry of the system. This leads to a chiral bias when spin modulations become present during the switching of the CoFeB layer.

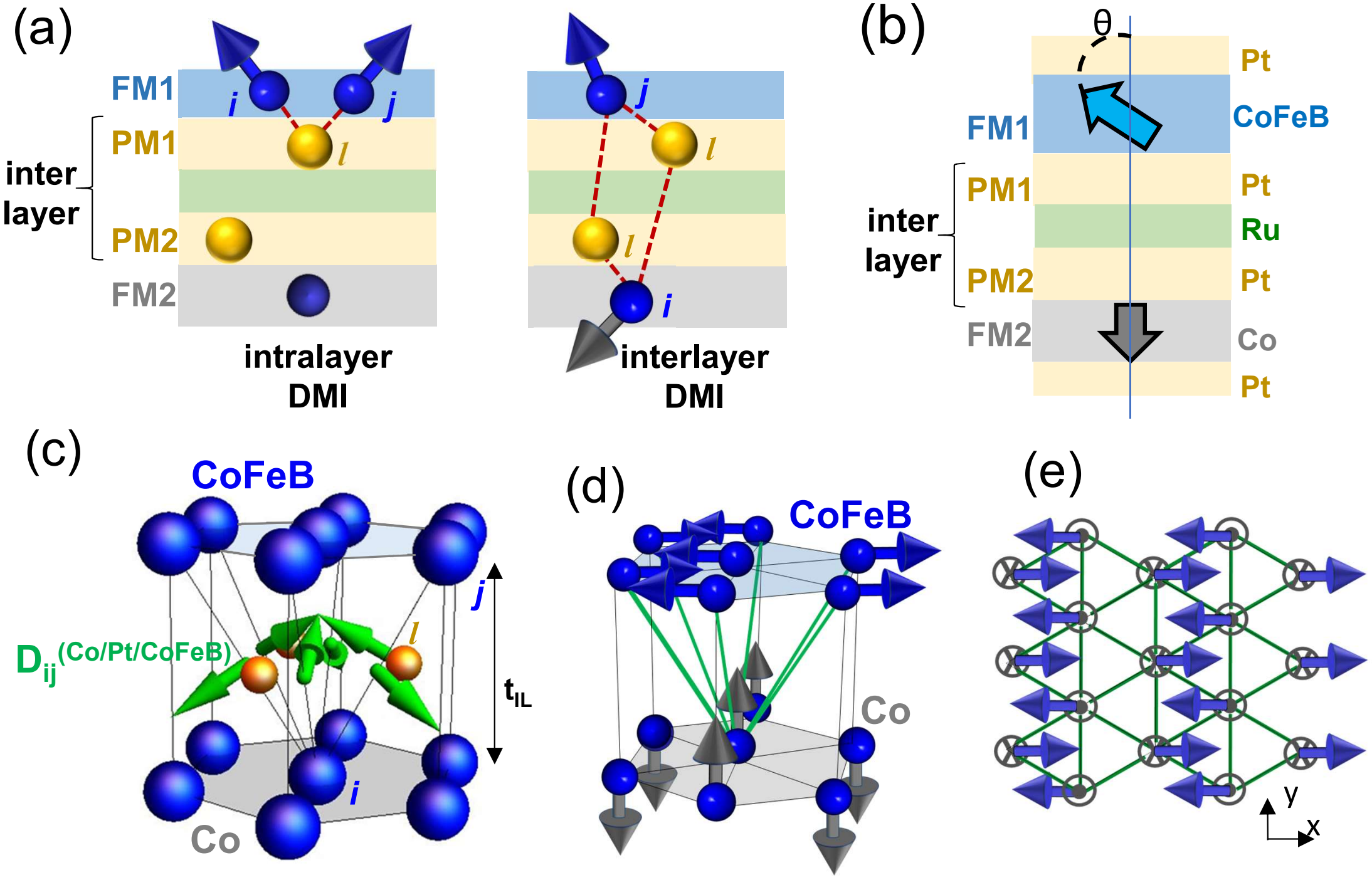
(a)
FM1
PM1
inter
layer
PM2
FM2
i
j
l
intralayer
DMI
interlayer
DMI
(b)
θ
Pt
CoFeB
FM1
PM1
Pt
inter
layer
Ru
PM2
Pt
FM2
Co
Pt
(c)
CoFeB
$D_{ij}^{(Co/Pt/CoFeB)}$
t_{IL}
Co
(d)
CoFeB
Co
(e)
y
x

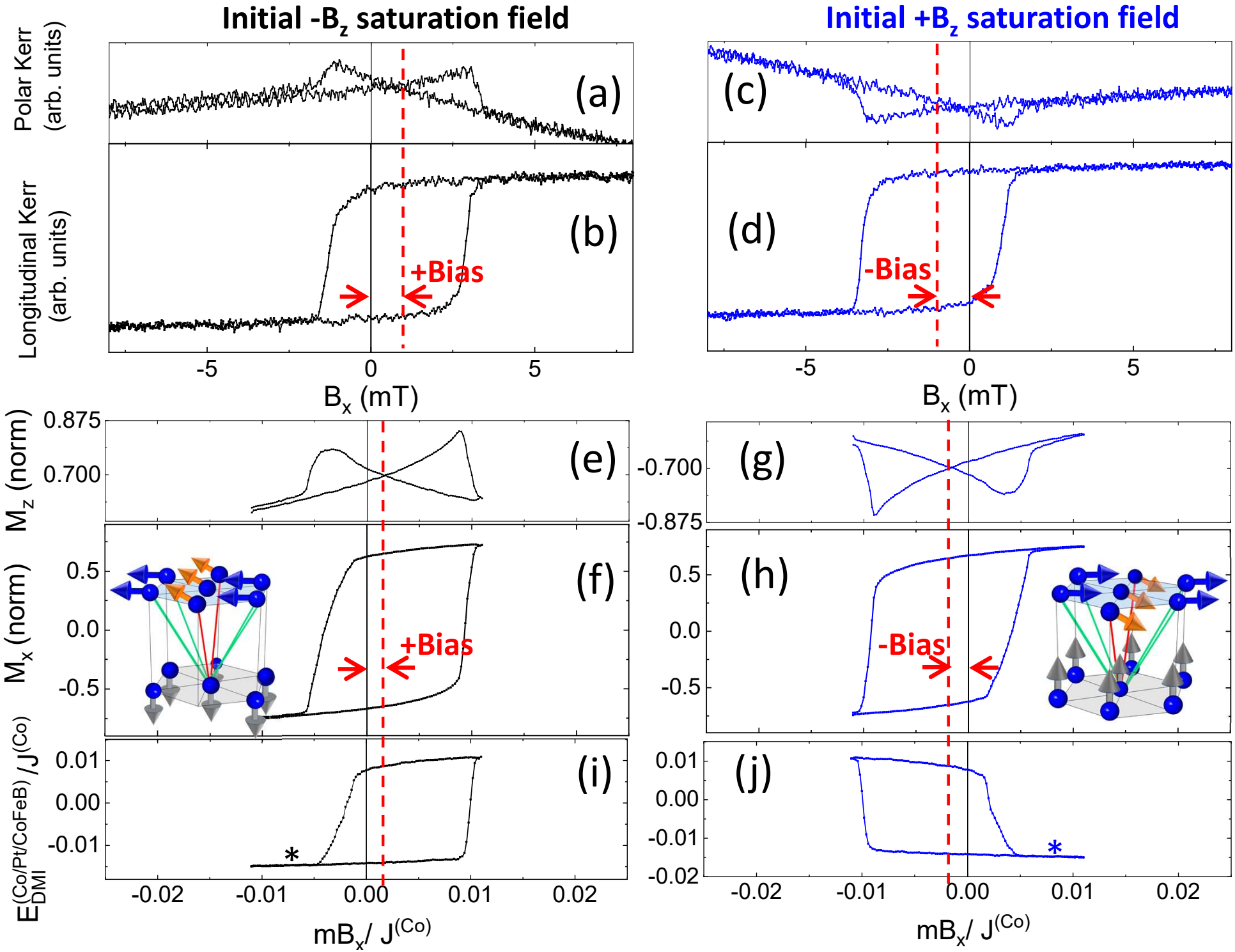
Initial -B$_z$ saturation field
Initial +B$_z$ saturation field
Polar Kerr (arb. units)
Longitudinal Kerr (arb. units)
(a)
(b)
(c)
(d)
+Bias
-Bias
B$_x$ (mT)
M$_z$ (norm)
M$_x$ (norm)
E$_{DMI}^{(Co/Pt/CoFeB)}$ /J$^{(Co)}$
(e)
(f)
(g)
(h)
(i)
(j)
mB$_x$/ J$^{(Co)}$

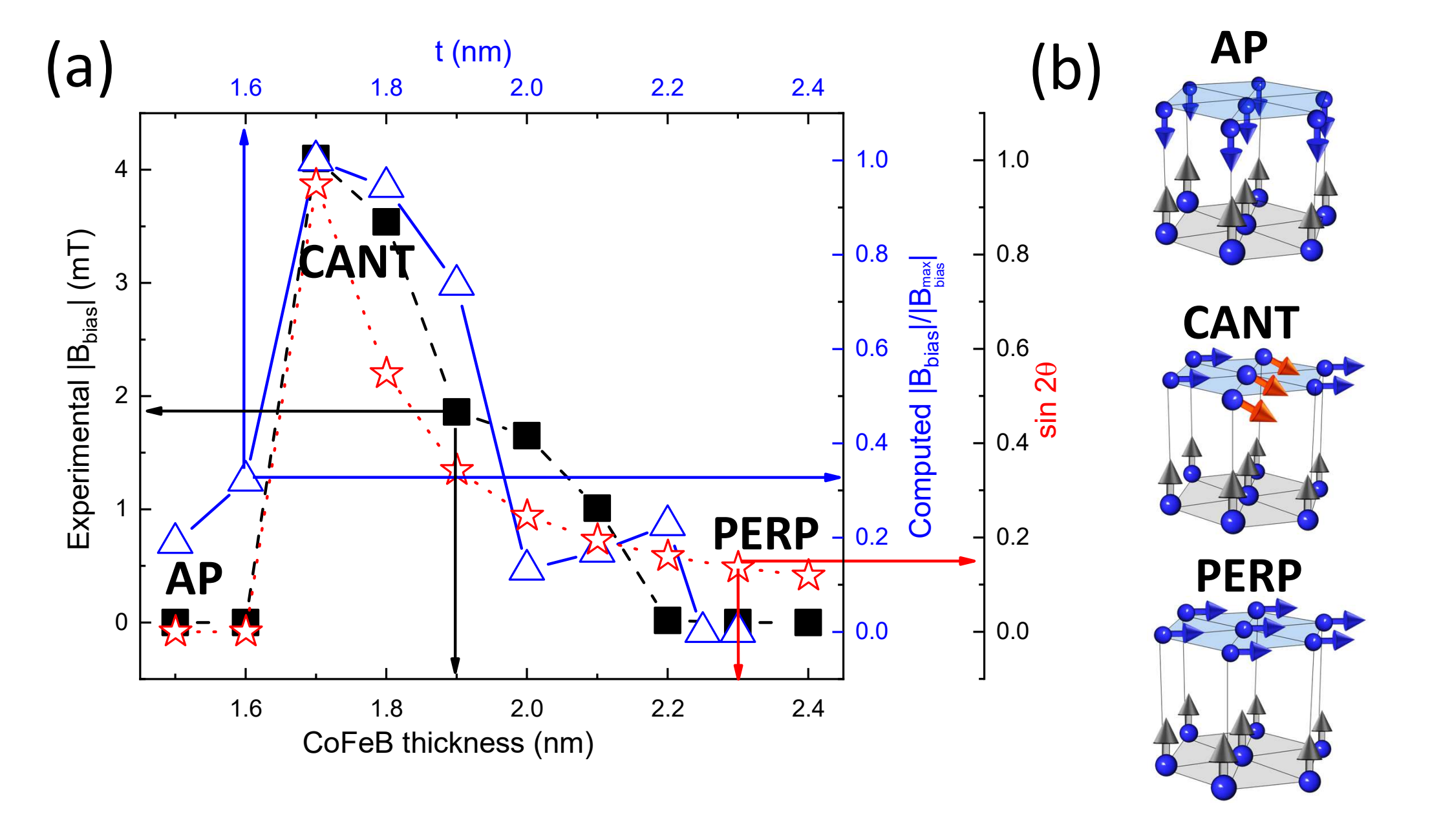
(a)
t (nm)
1.6
1.8
2.0
2.2
2.4
Experimental |B_bias| (mT)
Computed |B_bias|/|B_max bias|
sin 2θ
CANT
AP
PERP
CoFeB thickness (nm)
(b)
AP
CANT
PERP

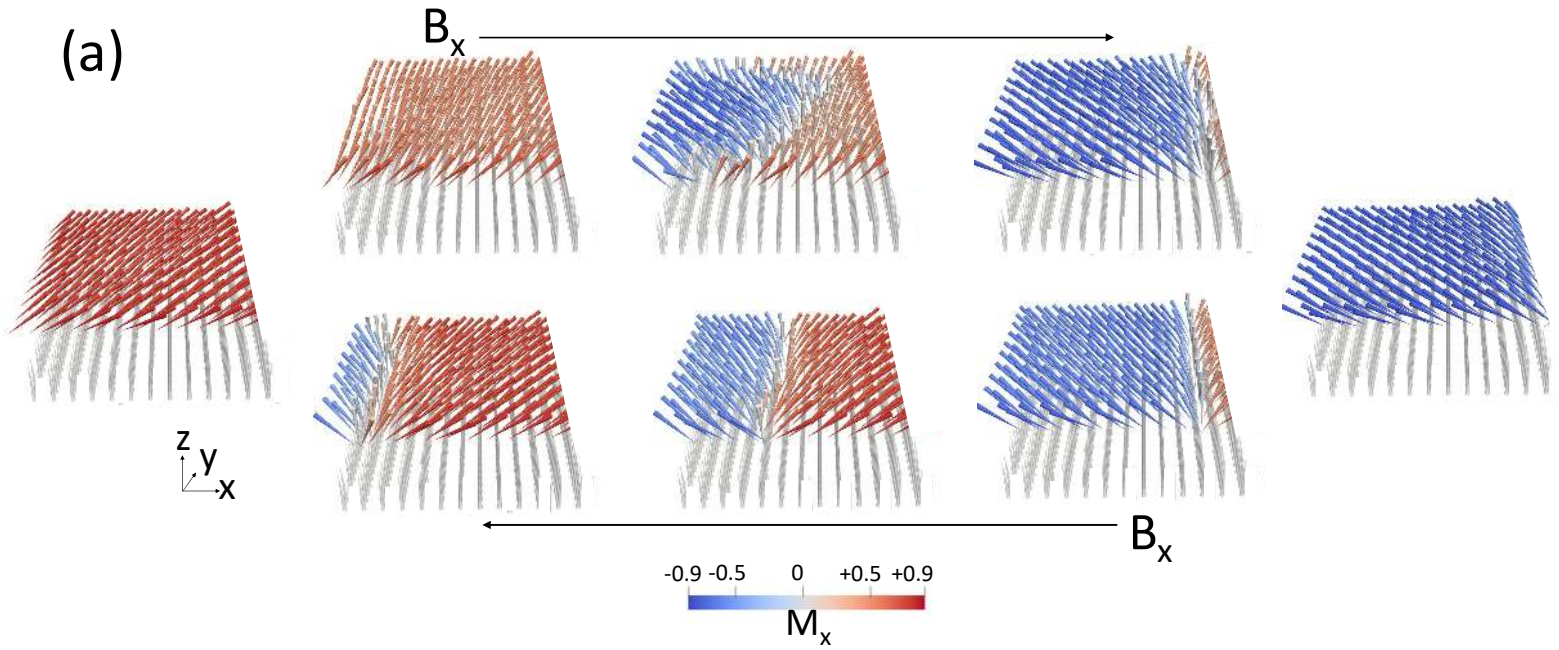
(a)
B_x
B_x
z
y
x
-0.9 -0.5 0 +0.5 +0.9
M_x

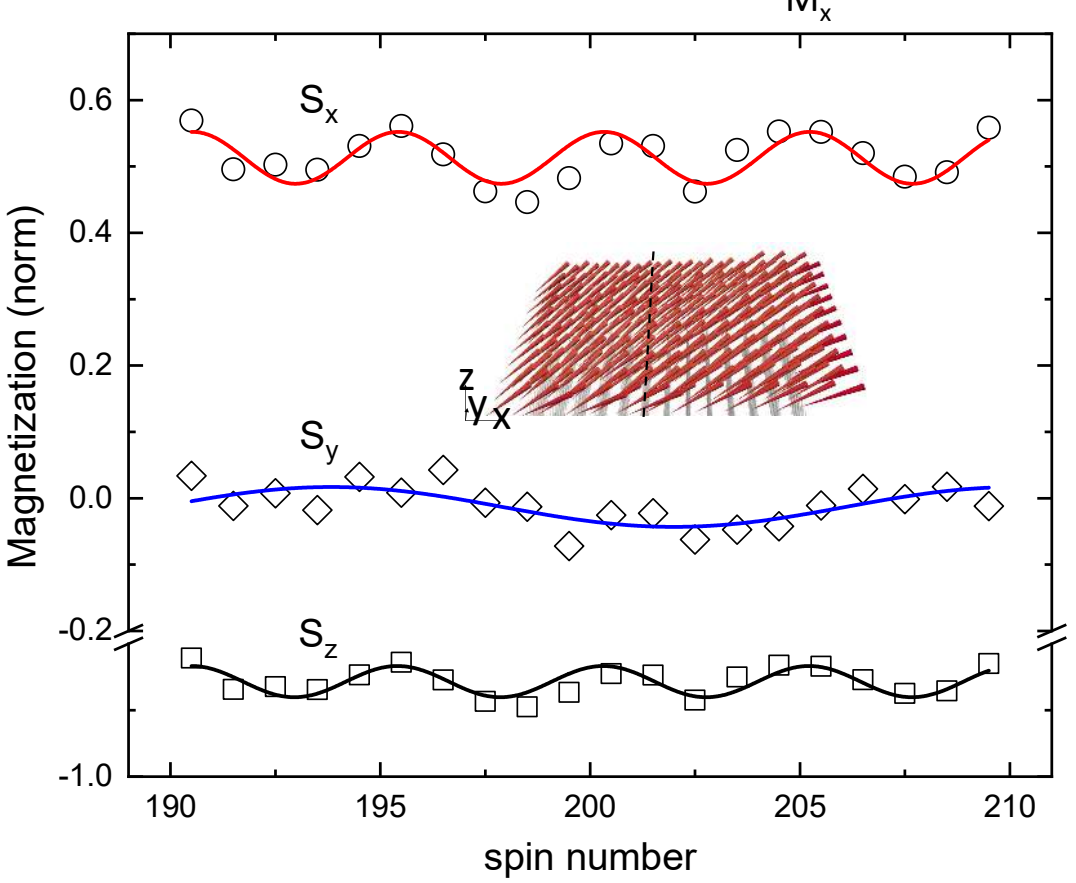
(b)
Magnetization (norm)
0.6
0.4
0.2
0.0
-0.2
-1.0
S_x
S_y
S_z
z
y
x
190
195
200
205
210
spin number

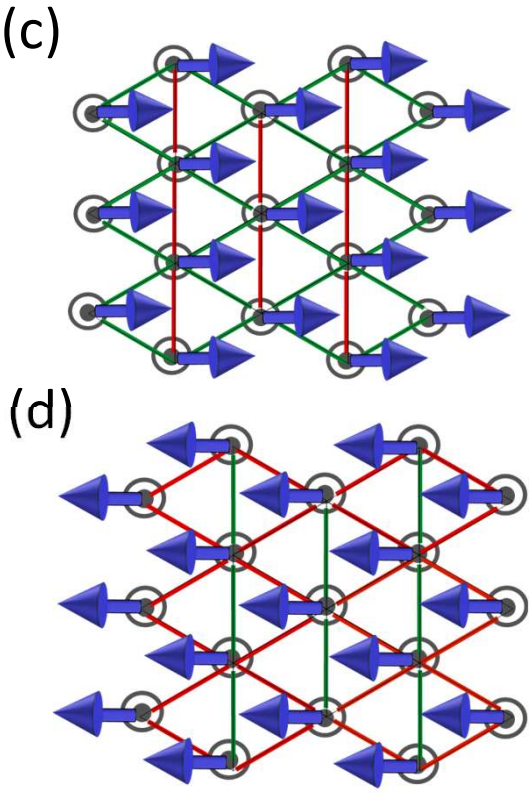
(c)
(d)